

Experimental and Numerical Investigations on the Dynamic Fracture of a Cylindrical Shell with Grooves Subjected to Internal Explosive Loading

Xiang Yu Li,^{*,[a, b, c]} Min Zhu Liang,^[a] Ma Fa Wang,^[a] Guo Xing Lu,^[b] and Fang Yun Lu^[a]

Abstract: A detailed experimental investigation on the dynamic fracture of a cylindrical shell with internal and external grooves subjected to internal explosive loading was carried out. Distributions of fragment velocities and fragment masses were measured and analyzed for specimens with different depths of the external grooves and different explosive materials, with the internal grooves of a fixed rectangular shape. Based on the experimental results, corresponding numerical simulations using the commercial software LS-DYNA were undertaken. By inspecting the fragments recovered from the experiments and the numerical results, the dynamic fracture of the casing led to fragments of approximately three shapes: a large cuboid fragment, a small cuboid fragment, and two irregular fragments

formed by three classical fracture trajectories. The formation mechanism of fragment shapes was analyzed using the fracture trajectories. A good agreement has been obtained between the numerical and experimental results. Finally, a parametric study for the casing thickness, grid patterns of the grooves and explosive materials was carried out in order to investigate the effects of fracture. The results showed that grid patterns of grooves and explosive materials had significant effects on the fracture mechanism of the casing. The numerical technique was used to predict the dynamic fracture of casing with internal and external grooves under internal explosive loading and for structural design in order to achieve desirable fragments with controlled shapes.

Keywords: Cylindrical shell • Groove • Fragment shape • Fracture trajectory • Internal explosive loading • Numerical simulation

1 Introduction

The cylindrical shell is used in a wide variety of engineering applications, from the containment pressure vessels of nuclear reactors to the elements of ammunition structure. The dynamic fracture of the casing subjected to internal explosive loading is a complex nonlinear problem. Fragmentation occurs due to an expansion of explosive-filled metal casing, usually dominated by classical fracture mechanics [1]. According to classical fracture mechanics, the fracture of the casing under internal explosive loading consists of tensile fracture and shear fracture [2]. Usually, the tensile fracture mode, where failure proceeds by crack propagation, is governed by the strain rate, the mass density, and the fracture energy per unit area (related to the material's fracture toughness), appearing on the external surface of the casing. Shear fracture is the second important mode of failure, which is initiated by adiabatic shear banding, which appears on the internal surface of the casing. Empirically, it is known that shear fracture is the dominant mode when the casing has fracture toughness and is not too thick.

The characteristics of the casing fracture, fragment velocities, fragment masses, and fragment shapes, depend on the explosive material and the casing geometry. Previous studies investigate the distribution of fragment velocity and mass. The distribution of fragment masses under inter-

nal loading was studied either analytically; see for example Mott [3], Grady [4,5], Zhang et al. [6] and Arnold et al. [7], or empirically reference [8]. With respect to the distribution of fragment velocities, the Gurney formula [9] provides an estimate of the fragment velocity for the casing as a function of the ratio between the explosive mass and that of the casing. Zhang et al. [10] and Tan et al. [11] presented a theoretical model to predict continuous deformation and acceleration of the casing driven by detonation products, respectively. Jaansalu et al. [12] investigated distribution of fragment velocities and fragment masses subjected to

[a] X. Y. Li, M. Z. Liang, M. F. Wang, F. Y. Lu
College of Science
National University of Defense Technology
Changsha 410073, P. R. China
*e-mail: xiangyu_lee@163.com

[b] X. Y. Li, G. X. Lu
School of Mechanical and Aerospace Engineering
Nanyang Technological University
Singapore 639798, Singapore

[c] X. Y. Li
State Key Laboratory of Explosion Science and Technology
Beijing Institute of Technology
Beijing 100081, P. R. China

thermo-baric explosives loading. Wang et al. [13] presented a formula to predict the radial distribution of the fragment velocities. Most fragments have irregular shapes resulting in high drag coefficients and large impact cross-sections, which decrease the warhead lethality especially at large distance.

In order to control the distribution of fragment masses and provide the desired terminal effects while retaining survivability, some techniques for controlled fragmentation were investigated. The most common technology for controlling fragmentation is based on grooves on the internal surface of the casing, obtained by machining or other techniques, for example laser and chemical. Pearson [14] used a grid system, which is usually machined into the inner surface of the warhead case. Arnold [15] presented a double casing structure to control the mass of fragment, the casing of the warhead divided into two concentric cylinders, with the external surface of the inner cylinder having a grid of grooves machined. These grooves have a depth of 1 mm and an asymmetrical V-shape notch. During the explosion, the sharp edges of the grooves hit the outer cylinder and indirectly control its fragmentation. Villano [16] verified the applicability of new technologies for manufacturing controlled fragmentation, focusing on four techniques: deep laser melting, laser micro-drilling, chemical treatment by nitration, and double casing. Hiroe et al. [17] analyzed the deformation and fragmentation behavior of metal cylinders, with different parameters such as wall thickness, wall materials, notches, and explosive-initiated locations. The main parameters of the controlled fragmentation are the geometric grid pattern of grooves along with their section profile. From the root of a groove with a symmetrical V-shaped notch, two orthogonal shear fractures can propagate, following the maximum shear trajectories with an angle of 45° with respect to the casing surface. From an asymmetrical V-shaped notch with a sharp tip at the root, a single shear fracture following the primary trajectory is propagated.

To date, the research on the controlled fragmentation is very limited. Most works focus on the casing material or the weakening technology. The purpose of this paper is to investigate the dynamic fracture of a casing with internal and external grooves under internal explosive loading. The distribution of fragment velocities and fragment masses was obtained experimentally. A corresponding numerical simulation was undertaken using LS-DYNA software. Fracture trajectories were analyzed using recovered fragments and modeling. Finally, a parametric study on the casing thickness, grid patterns of the grooves and explosive materials was carried out to analyze the effects of fracture. This study can be used to accurately predict the dynamic fracture of a casing with internal and external grooves under internal explosive loading, and can be used in structural design for controlled fragments shapes.

2 Experimental Procedure

2.1 Specimens

In order to investigate the dynamic fracture of the casing with grooves subjected to internal explosive loading, experiments were conducted. A schematic assembly is shown in Figure 1. The specimen consists of a cylindrical explosive charge, a casing, a skin, a booster, and two end-plates. The explosive charges used in the tests were TNT and Composition B (Comb.B) charges (= RDX/TNT 60/40) with a radius of 50 mm and a height of 50 mm. The charges were point-initiated with a column PETN booster (diameter 24 mm \times 15 mm) from the top center. The detonation wave and gas products become the drivers for the casing.

Each casing with internal and external grooves, made from 1020 steel, with an inner radius r_0 of 50 mm, a height of 10 mm, and a wall thickness t of 10 mm. The internal groove profile is rectangular, fixed at 2 mm deep d_i and 1 mm wide w_i on the inside wall surface. The external groove profiles on the outside wall surface are V-shaped with an included angle of 60° but different depths d_e . The angle θ of two adjacent internal grooves was evenly spaced at an angle of 18° , as were the external grooves. There are five identical casings stacked together in order, with all the grooves aligned. The thickness and the inner radius of the skin made from 1020 steel are 1 mm and 60 mm, respectively. Two end-plates of 10 mm thickness

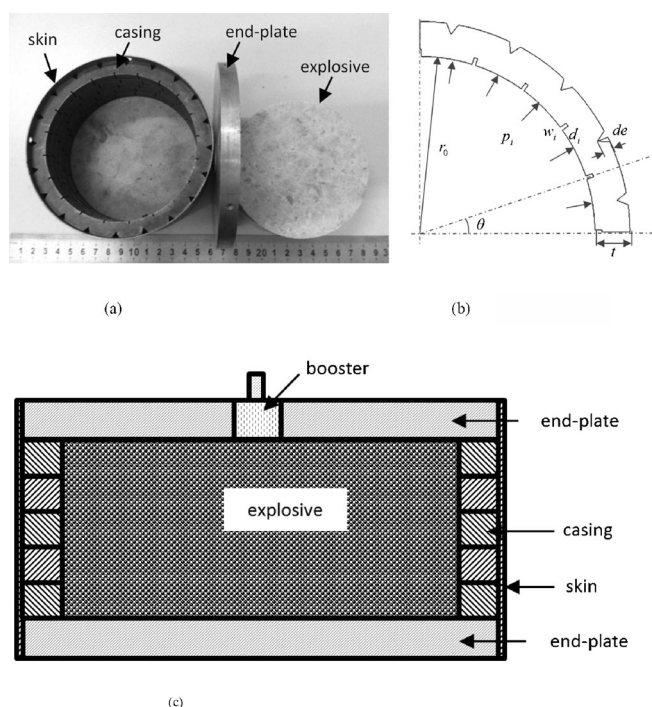


Figure 1. Specimen and assembly schematic of the experiments: (a) photograph of the experimental set-up consisting of cylindrical explosive, casing, skin, and end-plate. (b) Geometric parameter of the casing specimen. (c) Assembly schematic of the experimental set-up.

Table 1. Material properties of 1020 steel, LY12 aluminum.

Material names	Density [10 ³ kg m ⁻³]	Yield stress [MPa]	Young's modulus [GPa]	Poisson's ratio
1020 steel	7.85	275	210	0.29
LY12 aluminum	2.78	230	70	0.29

were made from LY12 aluminum and bolted to the skin in order to reduce the axial spread of detonation products. Material parameters and properties are listed in Table 1.

2.2 Experimental Set-up

During the experiments, fragment velocities, fragment shapes, and mass distributions were measured for all the tests. The experimental setup is shown in Figure 2.

Fragment velocities were measured using sensors of two copper foils separated by insulating foam. A signal was recorded when two copper foils were shorted by the penetration of a fragment. Based on the time between two signals over a known distance, the fragment velocity was calculated. The fragment was recovered using sandbags placed as a semi-circle at a distance of about 2.0 m away from the specimen. The sandbags were 1.0 m high and 0.3 m thick. In this way, the distribution of fragment masses was obtained, along with fragment shape while the fracture mechanisms were quantified based on the fragments recovered.

3 Experimental Results

The speed loss produced by air is a very important phenomenon, especially for the fragment lethality at large distances. This can be described by an exponential equation

$$v = v_0 e^{-kx} \quad (1)$$

where v is the fragment velocity at a distance x , v_0 is the initial velocity of the fragment, and k is a coefficient defined as

$$k = \rho A C_d / 2m \quad (2)$$

where ρ is the air density, A , C_d , and m are the cross-sectional area, the drag coefficient, and the mass of fragment, respectively. Based on the fragment shapes and masses recovered, the value of coefficient k can be calculated from Equation (2). Combined with the fragment impact velocities measured 2 m away, the initial fragment velocity can be obtained from Equation (1).

Most fragments could be recovered without any secondary damage for all the test conditions, from the semi-circle sandbags. Figure 3a–c shows photographs of typical fragments recovered after the tests with different depths ($d_e = 2.5$ mm, 4.0 mm) of the external grooves and two different explosive charges (TNT and Comp.B). The fragments in the photographs are placed from large to small ones. It is generally seen that there are two typical fragment shapes: large fragment and small fragment. All the fragments have the same thickness and height, and the arc length of the large fragment is approximately twice as much as for the small fragment. Therefore, the mass of the large fragment is approximately also twice of the small fragment, which has a mass of about 5 g. The fragment ratio is defined as the number of fragments recovered in the test over the possible number of fragments formed by the grooves. For example, for the TNT-R-T-3.0 experiment, in theory there should be 14 large fragments recovered, but only 8 fragments of NI were recovered from the experiment, and therefore the ratio of the large fragment RI is 57.1 %.

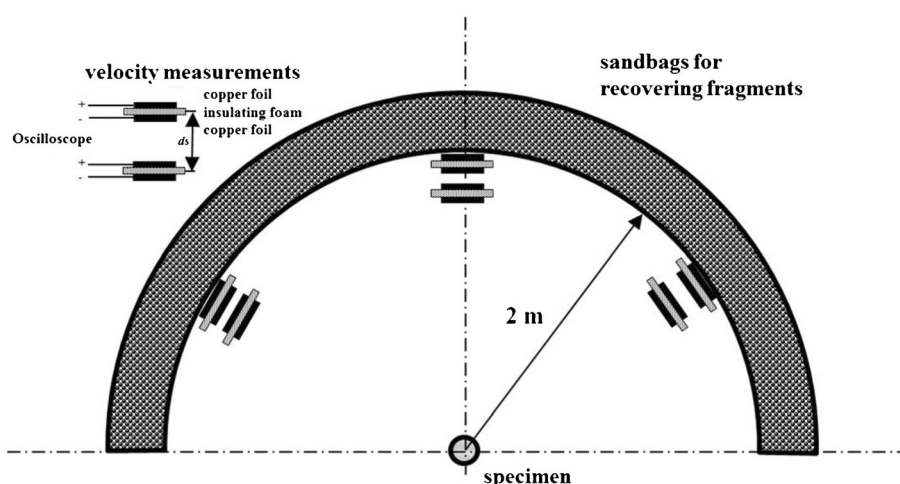


Figure 2. Sketch of the experimental set-up: the fragment impact velocities were measured by velocity measurements and the fragment shapes were recovered by semi-circle sandbags placed at a distance of 2.0 m from the specimen.

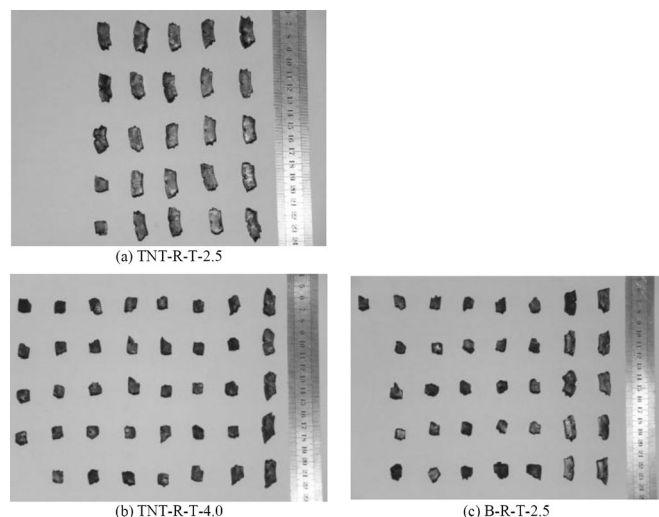


Figure 3. Photographs of typical fragments recovered after the tests: (a) and (b) with similar TNT explosive charge and five different groove depths ($d_e = 2.5$ mm, 4.0 mm, respectively), (c) and (b) with similar structure ($d_e = 2.5$ mm) and different explosive charges (TNT and Comp.B).

A summary of the experimental conditions, fragment masses, and fragment velocity is given in Table 2.

4 Finite Element Analysis

Based on the experimental arrangements, numeric simulations were carried out using LS-DYNA in order to study the dynamic fracture processes. LS-DYNA software was selected because it is a powerful tool for modeling non-linear mechanics. It has been widely used for analysis of dynamic problems associated with large deformation, low and high velocity contact/impact, ballistic penetration, and wave propagation.

4.1 Algorithm and Finite Element Model

The coupled Arbitrary-Lagrangian-Eulerian method (ALE) is used to analyze the dynamic processes of explosion driven

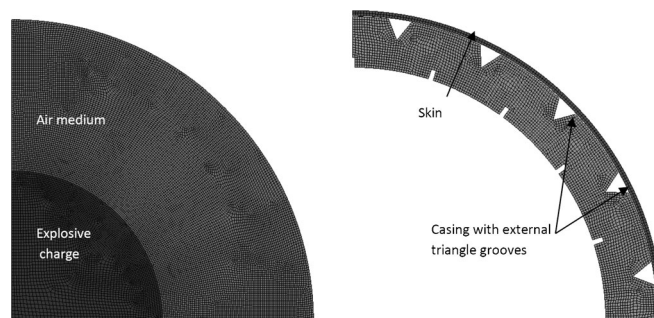


Figure 4. Cross-section profile of the finite element model: (a) Eulerian meshes, (b) Lagrangian meshes.

casing expansion. In the ALE model four different material models are employed; the first represents the explosive charge, the second the casing, the third the endplate, and the final one the surrounding air. The explosive charge and the air are set to Eulerian meshes, whereas the casing and endplate are set to Lagrangean meshes. The finite element model used in the simulations is shown in Figure 4. According to the inherent symmetries of xz plane and yz plane, only a quarter of the structure was modeled with appropriate boundary conditions applied along the symmetry planes. All the structures were meshed using eight-node brick (solid) elements with one integration point.

4.2 Materials Model and Parameters

In the simulations, the mechanical behaviors of LY12 aluminum was modeled with material type `**mat_plastic_kinematic` in LS-DYNA, which is a bi-linear elasto-plastic constitutive relationship that incorporates isotropic and kinetic hardening. The mechanical behaviors of 1020 steel was represented by the material type `**mat_elastic_plastic_hydro_spall`. The values of the material parameters are listed in Table 1. The shear fracture was modeled using `**mat_add_erosion`.

The material type `**mat_high_explosive_burn` was used to describe the material property of the explosive charge. It allows the modeling of detonation of a high explosive by three parameters: mass density of charge, detonation ve-

Table 2. Summary of experiments conditions and results ^{a)}.

Experiments no.	Explosive charge	External groove depth d_e [mm]	Number of large fragments N_l	Number of small fragments N_s	Ratio of large fragments R_l	Ratio of small fragments R_s	Fragment impact velocity v [km s ⁻¹]	Fragment initial velocity v_0 [km s ⁻¹]
TNT-R-T-2.0	TNT	2.0	23	5	90.2 %	9.80 %	1.19	1.22
TNT-R-T-2.5	TNT	2.5	23	2	95.8 %	4.20 %	1.20	1.23
TNT-R-T-3.0	TNT	3.0	8	12	57.1 %	42.9 %	1.23	1.27
TNT-R-T-3.5	TNT	3.5	2	10	28.6 %	71.4 %	1.21	1.24
TNT-R-T-4.0	TNT	4.0	5	34	22.7 %	77.3 %	1.25	1.28
B-R-T-2.5	Comp.B	2.5	10	26	43.5 %	56.5 %	1.55	1.59

a) d_e = external groove depth; N_l = number of large fragments; N_s = number of small fragments; R_l = ratio of the number of large fragment to the maximum possible number of such fragment; R_s = ratio of the number of small fragment to the maximum possible number of such fragment; v = fragment impact velocity; v_0 = fragment initial velocity;

locity, and Chapman-Jouget pressure. Likewise, an equation of state, named Jones-Wilkins-Lee (JWL) equation was used to define the explosive burn material model. This equation defines the pressure field as a function of relative volume and internal energy per initial volume

$$p = A \left(1 - \frac{\omega \rho}{R_1 \rho_0} \right) e^{-R_1 \frac{\rho}{\rho_0}} + B \left(1 - \frac{\omega \rho}{R_2 \rho_0} \right) e^{-R_2 \frac{\rho}{\rho_0}} + \frac{\omega \rho}{\rho_0} E_{m0} \quad (3)$$

where p is the detonation pressure, ρ is the explosive density, ρ_0 is the explosive density at the beginning of detonation process. The parameters A , B , R_1 , R_2 , and w are material constants, which are related to the type of explosive and can be found in most explosive handbooks. The air was modeled with a “*mat_null” and a linear polynomial EOS for linear internal energy. The material parameters of the TNT, Comp.B, and CL20 charges are listed in Table 3.

5 Numerical and Experimental Results

The perforation capability of the fragments on the target depends on the fragment properties (velocity, mass, and shape).

5.1 Distribution of Fragment Velocities

The Guerney formula gives a rough estimate of the fragments velocity as a function of the ratio between explosive and casing masses

$$v_0 = v_c (0.5 + M/C)^{-0.5} \quad (4)$$

where v_0 is the initial velocity of the fragments, v_c is the Guerney velocity (a constant for each explosive), M represents the casing mass, C is the explosive mass.

The fragment velocities can be calculated by Equation (3) at the different depths of external groove with the TNT charge. Figure 5 shows the initial velocity as a function of the ratio of the depth de of external groove to the casing thickness t . As the depth of external groove increases, the casing mass gradually reduces. The Guerney formula would predict the fragment velocity to increase with the reduction of casing mass. However, the effect of axial expansion of the detonation products is not taken into account, so the experimentally observed velocities obtained from the nu-

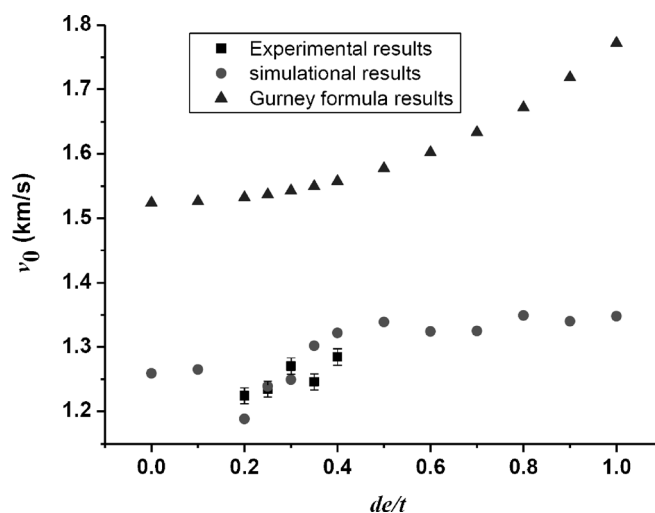


Figure 5. Distribution of the fragment initial velocities as a function of the ratio of the depth de of the external groove to the casing thickness t at similar TNT charge (cubes represent the calculated results of the Gurney formula, circles represent the experimental results, triangles represent the numerical results).

merical simulation and the experiment are lower than those from the Guerney formula. The increasing of the ratio of explosive mass to casing mass is counteracted by the expansion of detonation products through the fractures. Numerical results have a good agreement with the experimental results.

5.2 Distribution of Fragment Shapes

Based on the fragment shapes recovered, the dynamic fracture mechanism of the grooved casing is simulated using LS-DYNA software. There are three typical fracture trajectories: (1) fracture trajectory I, following the radial direction initiated at the root of internal groove; (2) fracture trajectory II, following the radial direction initiated at the root of external groove; (3) fracture trajectory III, following the direction between the root of internal and external groove. Schematics of fracture trajectories and fracture models are shown in Figure 6. In theory, fracture trajectories I and II occur with a possibility of 20 % each, and fracture trajectory III with a possibility of 40%.

Typical fragment shapes formed by different fracture trajectories are shown in Figure 7: a large fragment, a small fragment, and an irregular fragment. The large fragment is formed by two fracture trajectories I. The small fragment is

Table 3. Material properties of TNT, Comp.B, and CL20 charges [cm, g, μ s].

Material	Density	Detonation velocity	Detonation pressure	A	B (10^{-2})	R_1	R_2	w	E_0 (10^{-1})
TNT	1.63	0.69	0.21	3.73	3.75	4.15	0.90	0.35	0.60
Comp.B	1.72	0.80	0.29	5.24	7.68	4.20	1.10	0.34	0.85
CL20	1.94	0.92	0.39	1.64	186	6.50	2.70	0.55	1.15

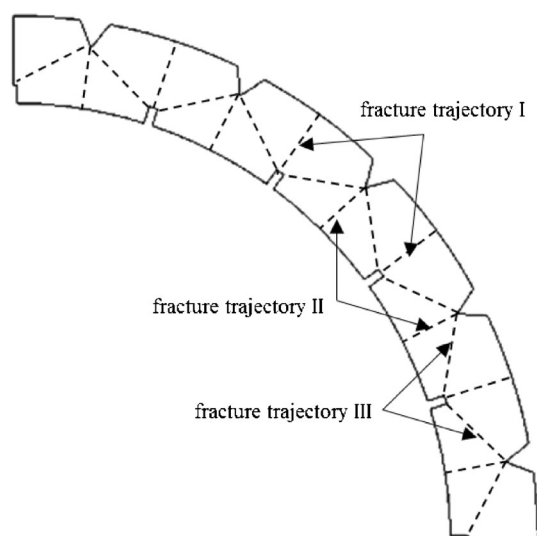


Figure 6. Distribution of fracture trajectories I, II, III for different structures: fracture trajectory I following the radial direction initiated at the root of internal groove; fracture trajectory II following the radial direction initiated at the root of external groove; fracture trajectory III following the direction between the root of internal and external groove.

generated by one fracture trajectory I and one trajectory II. The irregular fragment is formed by two fracture trajectories III in the material between external groove roots. The large fragment and the small fragment have the same thickness and height, the arc length of the large fragment is about twice than the small fragment. Two irregular fragments have the same height, the thickness related to the depth of external groove, and the length of inner and outer irregular fragment are equal to the length of adjacent internal and external grooves, respectively.

Figure 8 shows the experimental and numerical results of the ratios of fracture trajectories for different ratios of depth d_e (2.0 mm, 2.5 mm, 3.0 mm, 3.5 mm, 4.0 mm, respectively) of the external groove to casing thickness t at a given TNT charge. In Figure 8, solid lines and solid symbols represent the experimental results, and dotted lines and hollow symbols represent the numerical results. The data points are very close to the experimental results. When the ratio of the depth d_e of external to the casing thickness t has a value of 0.30, the numerical result indicates that the ratio of the number of fracture trajectory I to the maximum possible number of such fracture trajectory is 1, and for trajectory II and III 0.65 and 0, respectively. The experimental results of the ratio of fracture trajectory I, II, III are 1, 0.43, and 0, respectively, which denote relatively good agreement.

For the three fracture trajectories, the casing forms all predicted large fragments when the ratio of the groove depth to the casing thickness is below 0.25, while small fragments are generated only when the ratio of the groove depth d_e to the casing thickness t is equal to 0.5. Irregular

fragments formed as predicted when the ratio of the groove depth to the casing thickness is 0.6. In all other cases, the fragments formed have a mixture of large fragments, small fragments and irregular fragments. Therefore, different fragment shapes can be achieved by controlling the depth d_e of the external groove.

When the external grooves are shallow, the stress concentration is smaller, the crack initiation is more difficult and the crack propagation is slower, resulting in larger fragments. When the depth of external grooves is bigger, the stress concentration at external groove is larger, crack initiation is easier, and propagation is faster. Cracks from internal and external grooves extend through thickness almost simultaneously, and small fragments are formed. Appropriately adjusting the depth of external grooves leads to converging stress concentrations of external and internal grooves and formation of irregular fragments.

6 Parametric Studies

Fracture trajectories have a significant relationship with the casing thickness, grid pattern of grooves, and explosive materials. In order to better understand the fracture mechanism, a parametric study for the fracture trajectories is carried out and the results are discussed.

6.1 Effect of the Casing Thickness

For TNT charge and an interval angle of 18° between adjacent grooves, the distribution of three fracture trajectories with different ratio of groove depth d_e to casing thickness t is shown in Figure 9; casing thicknesses of 10 mm and 20 mm were used.

With an increasing ratio of groove depth to casing thickness at a casing thickness of 20 mm, the ratio of fracture trajectory I starts to decrease earlier, and those of fracture trajectories II and III start to increase earlier. When the casing thickness is equal to 20 mm, no small fragments are formed.

6.2 Effect of Grid Patterns of Grooves

In order to study the characteristics of the grid patterns of grooves, the finite element models were established. The distributions of fracture trajectories could be obtained at varying angles θ (15° , 18° , 22.5° , 30° , 45°).

Figure 10 shows the numerical results for the fracture trajectories with different groove depth to the casing thickness ratios at different interval angles θ for a fixed TNT charge. From the numerical results, fracture trajectory III is initiated when the interval angle is above 22.5° . When the ratio of the groove depth to the casing thickness is below 0.2, large fragments are formed only by fracture trajectory I. When this ratio is above 0.5, large fragments are generated by fracture trajectory II. A distribution of various frag-

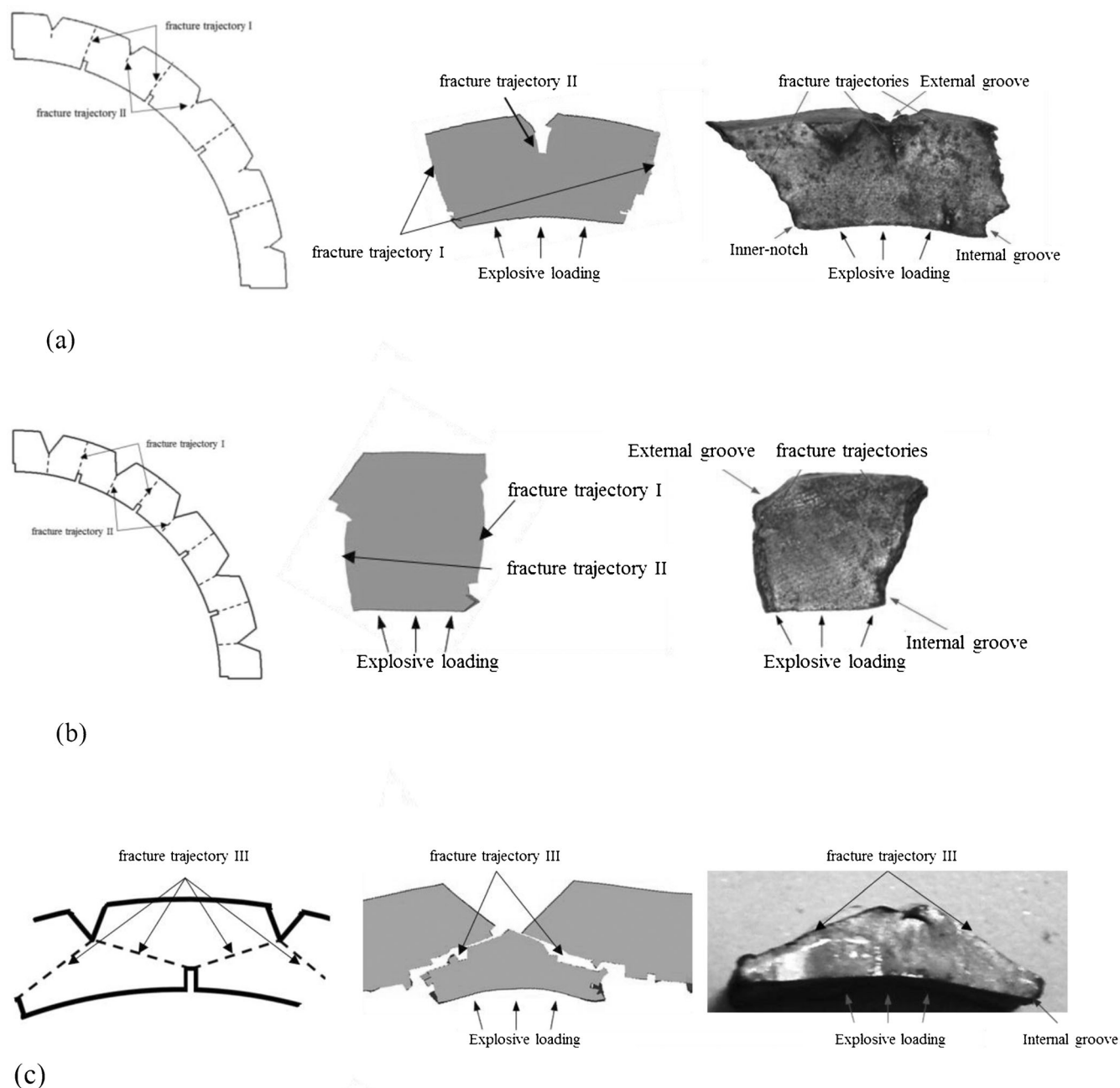


Figure 7. Typical fragment shapes: (a) large fragment formed by two (through casing thickness) adjacent trajectories I; (b) small fragment formed by two (through casing thickness) adjacent trajectories I and II; (c) irregular fragment formed by two (through length between internal and external grooves) adjacent trajectories III.

ment shapes can be achieved by adjusting the groove depths and interval angles between grooves.

6.3 Effect of Explosive Materials

In order to investigate the distribution of fracture trajectories of the grooved casing subject to different explosive

charges, three explosive charges (TNT, Comp.B, and CL20) were simulated. Figure 11 shows the numerical results. From the distribution of fracture trajectories within the specimens, as the detonation pressure of explosive charge increases, the ratio of fracture trajectory I starts to decrease at lower values of de/t . However, for fracture trajectory III, it starts to increase at larger values of de/t . This difference

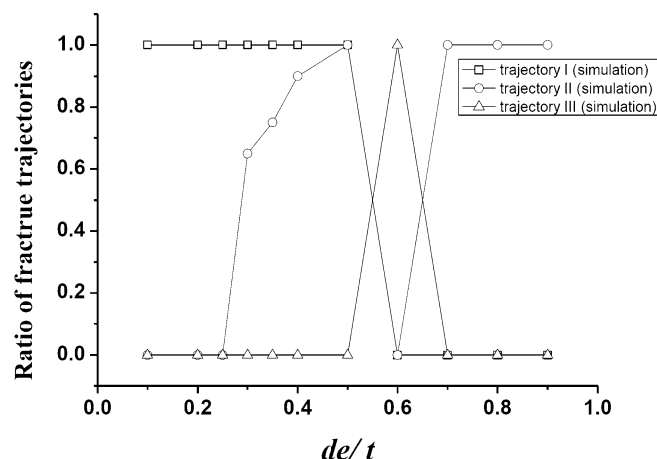


Figure 8. Numerically predicted ratio of fracture trajectories for different ratios of the depths de (2.0 mm, 2.5 mm, 3.0 mm, 3.5 mm, 4.0 mm, respectively) of external groove to casing thickness t at similar TNT charge (solid lines and solid symbols represent the numerical results).

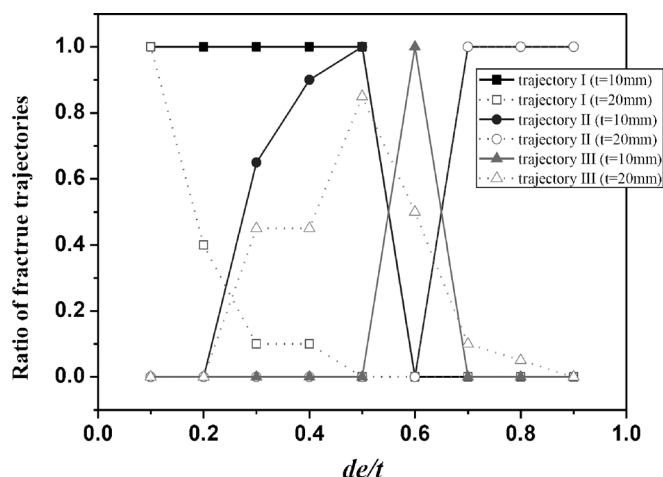


Figure 9. Numerical results of the ratio of fracture trajectories as a function of the ratio of the depth de of external groove to the casing thickness t , at similar TNT charge (solid lines and solid symbols represent casing with a thickness of 10 mm; dotted lines and hollow symbols represent casing with a thickness of 20 mm).

may be attributed to the fracture mechanism of the grooved casing. When the casing occurs at lower detonation pressure, the shear fracture is small. However, for higher detonation pressures, the shear stress is large, which leads to shear fracture.

7 Conclusion

The dynamic fracture of casings with internal and external grooves under internal explosive loading was studied.

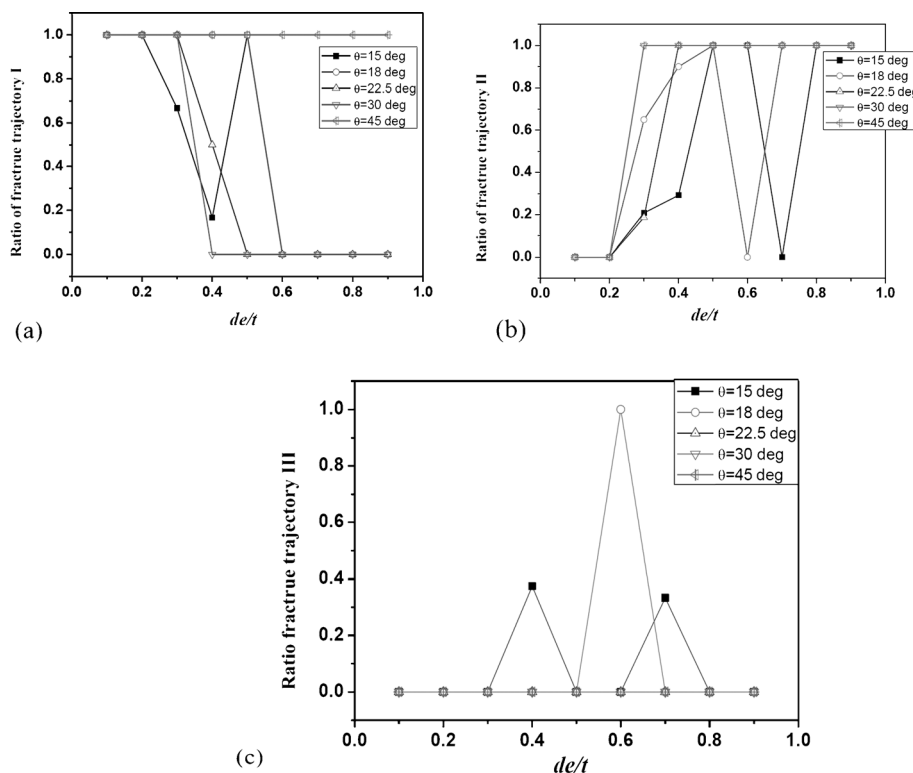


Figure 10. Numerical results of the ratio of fracture trajectories as a function of the ratio of the depth de of external groove to the casing thickness t , at different interval angles ($\theta = 15^\circ, 18^\circ, 22.5^\circ, 30^\circ, 45^\circ$): (a) ratio of fracture trajectory I, (b) ratio of fracture trajectory II, (c) ratio of fracture trajectory III.

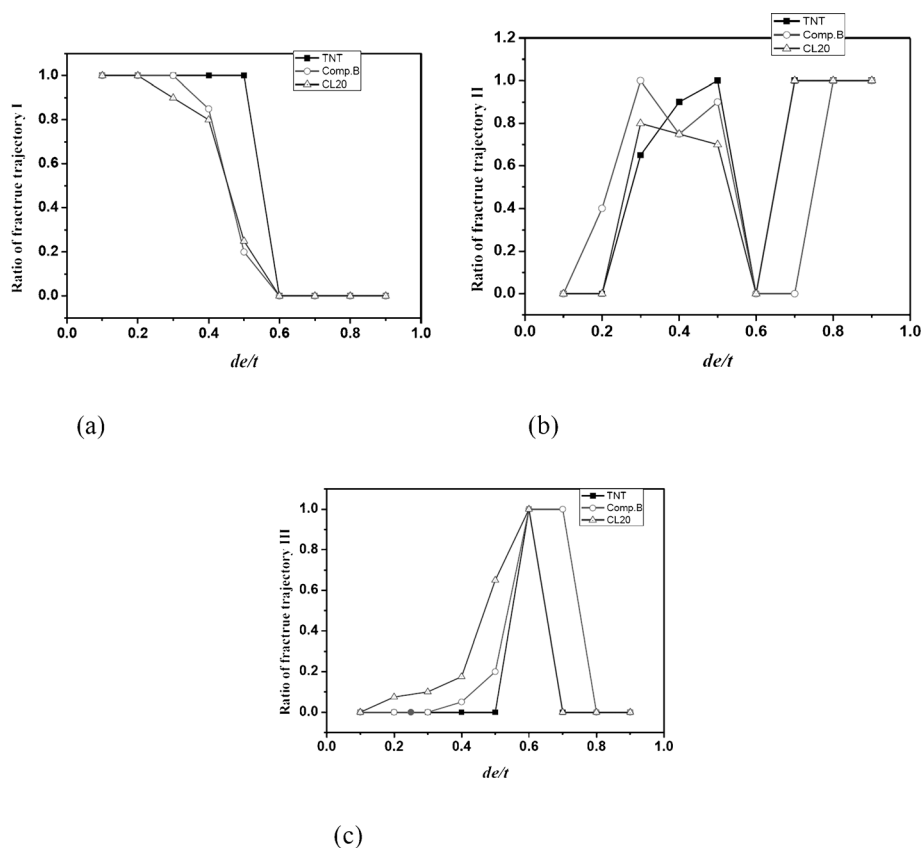


Figure 11. Distributions of the ratio of fracture trajectories as a function of the ratio of the depth de of external groove to the casing thickness t , with different explosive materials (TNT, Comp.B, and CL20): (a) ratio of fracture trajectory I, (b) ratio of fracture trajectory II, (c) ratio of fracture trajectory III (solid lines and solid symbols represent the numerical results).

Based on the experimental results, a corresponding numerical simulation using LS-DYNA software was presented.

There are three different types of fracture trajectories of a cylinder with grooves: (1) radial fracture initiated from the root of the internal grooves; (2) radial fracture from the root of external grooves; (3) fracture along the path between the roots of adjacent internal and external grooves. The numerical results of the fracture trajectories are similar to the experimentally observed. Meanwhile, a good agreement between the simulation and the experiments in terms of the fragment velocity and mass distribution was obtained.

A parametric study was conducted to analyze the factors influencing the fracture trajectories and fragment mass distribution. The results show that the explosive charge, the groove grid patterns, as well as the thickness of cylinder have significant effects on the fragments. The present simulation study can be used as a valuable tool to accurately predict the dynamic fracture of casing with internal and external grooves under internal explosive loading, and offers a guide for structural design of casing with internal and external grooves in order to obtain desirable fragments.

Acknowledgments

The authors acknowledge financial support by the National Natural Science Foundation of China under grant Nos. 11202237 and 11132012, and the State Key Laboratory of Explosion Science and Technology Opening Fund under grant No. KFJJ12-16MM.

References

- [1] J. Pearson, *A Fragmentation Model for Cylindrical Warheads*, Report No. NWC-TP-7124, Naval Weapon Center, China Lake, CA, USA, **1990**.
- [2] B. F. Wang, Y. Yang, Z. P. Chen, Y. Zeng, Adiabatic Shear Bands in α -Titanium Tube under External 3, *J. Mater. Sci.* **2007**, *42*, 8101–8105.
- [3] N. F. Mott, Fragmentation of Shell Cases, *Proc. R. Soc. Lond. A* **1947**, *189*, 300–308.
- [4] D. Grady, Fragmentation of Expanding Cylinders and the Statistical Theory of N. F. Mott, *12th Conference of the American Physical Society Topical Group on Shock Compression of Condensed Matter*, Atlanta, GA, USA, June 24–29, **2001**, AIP Conference Proceedings 620, pp. 799–802.

- [5] D. E. Grady, Fragment Size Distributions from the Dynamic Fragmentation of Brittle Solids, *Int. J. Impact Eng.* **2008**, 35, 1557–1562.
- [6] L. Zhang, X. G. Jin, H. L. He, Prediction of Fragment Number and Size Distribution in Dynamic Fracture, *J. Phys. D* **1999**, 32, 612–615.
- [7] W. Arnold, E. Rottenkolber, Fragment Mass Distribution of Metal Cased Explosive Charges, *Int. J. Impact Eng.* **2008**, 35, 1393–1398.
- [8] U. Günther, N. Heider, Application of an Empirical Number and Mass Distribution for Natural Fragments to the Estimation of their Target Effectiveness, *Propellants Explos. Pyrotech.* **1998**, 23, 159–163.
- [9] R. W. Gurney, *The Initial Velocities of Fragments from Bombs, Shells and Grenades*, BRI Report NO 405, Ballistic Research Laboratory, Aberdeen Proving Ground, MD, USA, **1943**.
- [10] Q. Zhang, C. Q. Miao, D. C. Lin, C. H. Bai, Relation of Fragment with Air Shock Wave Intensity for Explosion in a Shell, *Int. J. Impact Eng.* **2003**, 28, 1129–1141.
- [11] D. W. Tan, C. W. Sun, Y. P. Wang, Acceleration and Visco-Plastic Deformation of Spherical and Cylindrical Casings under Explosive Loading, *Propellants Explos. Pyrotech.* **2003**, 28, 43–47.
- [12] K. M. Jaansalu, M. R. Dunning, W. S. Andrews, Fragment Velocities from Thermo-baric Explosives in Metal Cylinders, *Propellants Explos. Pyrotech.* **2007**, 32, 80–86.
- [13] M. F. Wang, F. Y. Lu, X. Y. Li, L. Cao, A Formula for Calculating the Velocities of Fragments from Velocity Enhanced Warhead, *Propellants Explos. Pyrotech.* **2013**, 38, 232–237.
- [14] J. Pearson, The Shear Control Method of Warhead Fragmentation, *4th International Symposium on Ballistics*, Monterey, CA, USA, October 17–19, **1993**.
- [15] W. Arnold, Controlled Fragmentation, *12th Conference of the American Physical Society Topical Group on Shock Compression of Condensed Matter*, Atlanta, GA, USA, June 24–29, **2001**, AIP Conference Proceedings 620, pp. 527–530.
- [16] D. Villano, F. Galliccia, Innovative Technologies for Controlled Fragmentation Warheads, *Int. J. Appl. Mech. Eng.* **2013**, 80, 031704–1–9.
- [17] T. Hiroe, K. Fujiwara, H. Hata, H. Takahashi, Deformation and Fragmentation Behavior of Exploded Metal Cylinders and Effects of Wall Materials, Configuration Explosive Energy and Initiated Locations, *Int. J. Impact Eng.* **2008**, 35, 1578–1586.

Received: September 27, 2013

Revised: March 2, 2014

Published online: April 30, 2014